J Adv Ceram

Research Article

Thickness-regulated interfacial polarization in CTAB-tailored Bi_2WO_6 for enhanced piezocatalysis

Xiaoli Xu[1,2,†], Ying Wang[1,†], Wanwan Cheng[1,†], Huan Zhai[1], Jinqian Ma[1], Lingbo Xiao[3,✉], Laishun Qin[1,✉], Wenwen Liu[4], Yanmin Jia[5], Zhenhai Wen[2,6], Da Chen[1,✉]

Cite this article: Xu X, Wang Y, Cheng W, et al. *J Adv Ceram* 2026, **15**(3): 9221255. https://doi.org/10.26599/JAC.2026.9221255

ABSTRACT: While morphology regulation in conventional catalysis mainly increases the specific surface area to expose more active sites, in piezocatalysis, it additionally alters the polarization properties of the materials. In this work, by leveraging the dual benefit of morphology regulation in piezocatalysis, we used cetyltrimethylammonium bromide (CTAB) to synthesize two-dimensional ultrathin Bi_2WO_6 (BWO) nanosheets, whose minimal thickness of ~2.26 nm results from the selective adsorption of CTAB inhibiting molecular layer stacking. This morphological control not only increased the specific surface area by more than doubling from 14.47 to 29.15 $m^2 \cdot g^{-1}$ but also enhanced the interfacial polarization by 18.34 mV. Consequently, the effective piezoelectric coefficient of CTAB-modified BWO rose from ~10.01 to ~27.53 $pm \cdot V^{-1}$. The modified catalyst, by simultaneously increasing reactive sites and boosting piezoelectric performance, achieves a maximum per-unit-power hydrogen production rate of 61.20 $\mu mol \cdot g^{-1} \cdot h^{-1} \cdot W^{-1}$, which is one of the highest values ever reported. This work demonstrates a synergistic strategy of morphology engineering to enhance the surface reactivity and piezoelectric response, offering a new paradigm for high-performance piezocatalysts.

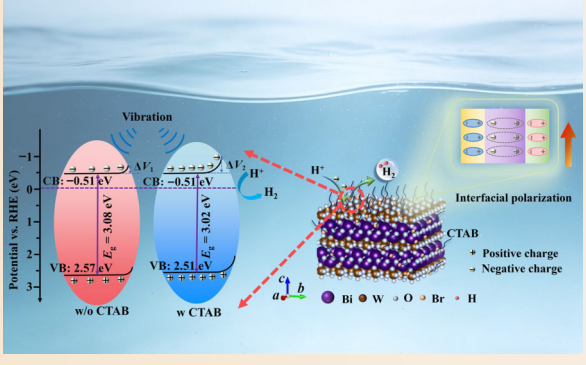

KEYWORDS: thickness regulation; interfacial polarization; piezoelectric coefficient; piezocatalytic hydrogen generation

1 . Introduction

With the intensifying global energy crisis and increasingly prominent environmental issues, the path toward sustainable development of human society is fraught with severe constraints [1,2]. As an emerging catalytic approach, piezocatalytic hydrogen production utilizes ubiquitous mechanical energy to activate catalysts for redox reactions, offering a clean method that avoids secondary pollutant generation [3–6]. However, traditional piezocatalysts face challenges such as rapid recombination of piezo-induced charges ($q^+ - q^-$), which substantially limits their practical utility [7–9]. Therefore, enhancing charge carrier separation/transport efficiency and improving piezocatalytic performance remain critical focuses in current material modification research.

Active sites are pivotal for enhancing catalytic performance by facilitating charge transfer and separation through electron transport channels, which accelerates reaction kinetics and improves charge utilization [10]. Concurrently, they optimize reactant adsorption and activation, thereby lowering the activation energy barrier [11]. Morphology regulation is an effective strategy for increasing the specific surface area (S_{BET}), which enhances catalytic performance by exposing more active sites and providing abundant venues for charge-reactant interactions [12,13]. Zhao *et al.* [14] found that ultrathin BiOBr nanosheets exhibited exceptional photocatalytic performance due to a reduced bandgap (E_g) and accelerated photoinduced charge transfer after morphology regulation. Abbood *et al.* [15] found that a reduced thickness of CdS nanosheets enhances the S_{BET} and increases the active site density, thereby improving the piezoelectric/

† Xiaoli Xu, Ying Wang, and Wanwan Cheng contributed equally to this work.

[1] College of Materials and Chemistry, China Jiliang University, Hangzhou 310018, China. [2] Key Laboratory of Jiangxi Province for Persistent Pollutants Control, National-Local Joint Engineering Research Center of Heavy Metals Pollutants Control and Resource Utilization and Resources Recycle, Nanchang Hangkong University, Nanchang 330063, China. [3] Department of Physics, Zhejiang University of Science and Technology, Hangzhou 310008, China. [4] Key Laboratory of Lithium Battery New Energy Materials and Devices of Jiangxi Education Department, College of Intelligent Manufacturing and Materials & Chemical Engineering, Yichun University, Yichun 336000, China. [5] School of Physics and Information Technology, Shaanxi Normal University, Xi'an 710121, China. [6] State Key Laboratory of Structural Chemistry, Fujian Provincial Key Laboratory of Materials and Techniques toward Hydrogen Energy, Fujian Institute of Research on the Structure of Matter, Chinese Academy of Sciences, Fuzhou 350002, China.

✉ Corresponding authors. E-mail: L. Xiao, lbxiao@zust.edu.cn; L. Qin, qinlaishun@cjlu.edu.cn; D. Chen, chenda@cjlu.edu.cn

Received: December 28, 2025; Revised: January 10, 2026; Accepted: January 26, 2026

photocatalytic activity. Hu *et al.* [8] found that atomically thin graphite carbon nitride (g-C_3N_4) nanosheets demonstrated approximately 5 times piezocatalytic performance superior to that of bulk g-C_3N_4 due to the increased number of surface reaction sites.

Furthermore, in mechanically induced catalysis, reducing the thickness of catalysts enhances the flexibility, making them more susceptible to bending or deformation and thus facilitating the generation of electric charges [16,17]. Feng *et al.* [18] utilized ZnS nanosheets (~2 nm, ~18 pC·N^{-1}) for piezocatalytic water splitting. The resulting ultrathin structure is highly susceptible to bending under ultrasonic vibration, a property that generates the necessary piezoelectric charges to drive hydrogen evolution from water. The polymer-like flexibility of ferroelectric $Hf_{0.5}Zr_{0.5}O_2$ subnanowires (~1 nm diameter) enables easy polarization switching under mechanical vibration, accounting for their exceptional piezocatalytic hydrogen production rate, which is 235 times higher than that of nonferroelectric HfO_2 [19]. While morphology regulation in conventional catalysis mainly increases the specific surface area to expose more active sites, in piezocatalysis, it additionally alters the polarization performance of the materials [20–22]. Finite element simulations by Li *et al.* [23] on a single SnSe few-layer nanosheet under 100 MPa pressure revealed a maximum piezoelectric potential of 44.1 V. To investigate the structure-activity relationship in piezocatalysis, Wang *et al.* [24] synthesized CdS nanorods and nanospheres and found that the nanorods exhibited a hydrogen evolution rate 2.8 times higher than that of nanospheres. This superior performance was attributed to the enhanced piezoelectric properties of nanorods, stemming from their one-dimensional structure, which provides a higher piezoelectric coefficient and superior mechanical strain collection, ultimately leading to a larger piezoelectric potential and more efficient charge separation and transfer.

Among various piezocatalysts, bismuth tungstate (Bi_2WO_6, BWO) is the simplest member of the Aurivillius oxide family, a class of layered perovskites with the general formula $Bi_2A_{n-1}B_nO_{3n+3}$ (where n = 1; A = Ca, Sr, Ba, Pb, Bi, Na, K; B = Ti, Nb, Ta, Mo, W, Fe). The crystal structure of BWO features alternating layers of perovskite-like $(WO_4)^{2-}$ and fluorite-like $(Bi_2O_2)^{2+}$ blocks. This unique layered structure endows BWO with distinctive physicochemical properties [25–27]. Nevertheless, conventional BWO materials suffer from insufficient active site exposure, significantly constraining their applications in piezocatalysis. Regulating the thickness of materials by adding surfactants is a common synthetic method for preparing ultrathin materials. The addition of surfactants is a common strategy for synthesizing ultrathin materials by regulating their thickness [28–30]. According to the reported literature, the main categories of surfactants used for regulating the thickness of BWO are shown in Table S1 in the Electronic Supplementary Material (ESM). Cetyltrimethylammonium bromide (CTAB) is a well-established cationic surfactant featuring a molecular architecture composed of a long hydrophobic alkyl chain, a hydrophilic trimethylammonium cationic headgroup, and a Br^-. Owing to this unique amphiphilic structure, CTAB tends to self-assemble into micelles and adsorption layers in aqueous or organic solvent systems. When Br^- ions were introduced in the synthesis system, they would bond to the exposed coordinatively unsaturated Bi atoms on the surface of BWO to terminate the dangling bonds partly, rendering the nanosheets negatively charged. Concurrently, the cationic CTA^+ species adsorbed *via* the bound Br^- ions. The resulting Coulomb repulsion forces, combined with the steric hindrance from the hydrophobic chains of the CTA^+ ions, effectively prevented the stacking of the nanosheets [29].

In this work, by leveraging the dual benefit of morphology regulation in piezocatalysis, we used CTAB to synthesize two-dimensional ultrathin BWO nanosheets, whose minimal thickness of ~2.26 nm results from the selective adsorption of CTAB inhibiting molecular layer stacking. This morphological control not only increased the specific surface area by more than doubling from 14.47 to 29.15 $m^2 \cdot g^{-1}$ but also enhanced the interfacial polarization by 18.34 mV. Consequently, the effective piezoelectric coefficient of CTAB-modified BWO rose from ~10.01 to ~27.53 $pm \cdot V^{-1}$. The modified catalyst, by simultaneously increasing reactive sites and boosting piezoelectric performance, achieves a maximum per-unit-power hydrogen production rate of 61.20 $\mu mol \cdot g^{-1} \cdot h^{-1} \cdot W^{-1}$, which is one of the highest values ever reported. This work demonstrates a synergistic strategy of morphology engineering to enhance the surface reactivity and piezoelectric response, offering a new paradigm for high-performance piezocatalysts.

2 Experimental

2.1 Chemical reagents

All materials and solvents were of analytical grade and were used without any further purification. Sodium tungstate dihydrate ($Na_2WO_4 \cdot 2H_2O$, ≥ 99.5%), methanol (MeOH, ≥ 99.5%), and anhydrous sodium sulfate (Na_2SO_4, ≥ 99.0%) were supplied by Shanghai Macklin Biochemical Co., Ltd. Bismuth (III) nitrate pentahydrate ($Bi(NO_3)_3 \cdot 5H_2O$, ≥ 99.0%) was purchased from Sinopharm Chemical Reagent Co., Lid. Cetyltrimethylammonium bromide (CTAB, 99.0%) was purchased from Aladdin Chemical Reagent Co., Ltd. (Shanghai, China). Anhydrous ethanol (C_2H_5OH, ≥ 99.7%) and deionized water were obtained from Hangzhou Mike Chemical Instrument Co., Ltd. Deionized water was used as the solvent throughout the experiments. Ethylenediaminetetraacetic acid (EDTA, ≥ 99.5%) was purchased from Tianjin Yongda Chemical Reagent Co., Ltd. Anhydrous sodium sulfite (Na_2SO_3, ≥ 97.0%) and triethanolamine (TEOA, AR) were obtained from Hangzhou Gaojing Fine Chemical Industry Co., Ltd. Rhodamine B (RhB, AR) was purchased from Tianjin Kermel Chemical Reagent Co., Ltd.

2.2 Sample preparation

BWO ultrathin nanosheets were synthesized via a CTAB-assisted hydrothermal method [31]. To synthesize CTAB-modified BWO, 0.33 g of $Na_2WO_4 \cdot 2H_2O$ and 0.1–0.4 g of CTAB were dissolved in 50 mL of deionized water under magnetic stirring to form Solution A, respectively. Subsequently, 0.97 g of $Bi(NO_3)_3 \cdot 5H_2O$ was added to Solution A, and the mixture was stirred until a homogeneous suspension (solution B) was obtained. Solution B was then transferred to a 100 mL Teflon-lined autoclave, filled with deionized water to two-thirds of its capacity, sealed, and maintained at 160 °C for 24 h. The resulting precipitate was collected, washed sequentially with anhydrous ethanol and deionized water, and dried at 60 °C to yield the final product. For comparison, pristine BWO was prepared following an identical procedure without the addition of CTAB (Fig. S1 in the ESM). Unless otherwise noted, the CTAB modification amount throughout the text is 0.3 g.

2.3 Structural and morphological characterization

X-ray diffraction (XRD) patterns were recorded on a Shimadzu Smart Lab-SE diffractometer (Ultima IV, Rigaku, Japan) with Cu Kα radiation (λ = 0.15406 nm), scanning from a 2θ range of 20° to

80° at 10 (°)·min^{-1}. The morphology and elemental distribution of the samples were investigated using a scanning electron microscope (SEM; Sigma 300, Carl Zeiss, Germany) equipped with an energy-dispersive X-ray spectrometer (EDS) for elemental mapping. The element contents were quantitatively determined by inductively coupled plasma spectrometry/mass spectrometry (ICP-MS) using an Agilent 7800 instrument (USA). High-resolution transmission electron microscopy (HRTEM) images were acquired using a Tecnai F30 instrument (FEI, USA) to observe lattice fringes and interplanar spacings. Aberration-corrected high-angle annular dark field scanning transmission electron microscopy (HAADF-STEM) images were obtained on a 300 kV aberration-corrected transmission electron microscope (JEMARM300F, JEOL, Japan). Atomic force microscopy (AFM), piezoresponse force microscopy (PFM) amplitude butterfly curves and Kelvin probe force microscopy (KPFM) measurements were performed using an atomic force microscope (Dimension Icon, Bruker, Germany). X-ray photoelectron spectroscopy (XPS) was conducted on a K-Alpha spectrometer (Thermo Fisher Scientific, USA) to analyze the surface elemental composition and valence states. All binding energies were calibrated using the C 1s peak at 284.8 eV as a reference. The Brunauer–Emmett–Teller (BET) specific surface area (S_{BET}) was determined by N_2 adsorption-desorption measurements at 77.30 K on an ASAP 2460 analyzer (Micromeritics, USA). Before analysis, samples were degassed at 200 °C for 7 h under vacuum. To measure the dielectric constant at room temperature, the powder sample was first pressed into a tablet, and electrodes were applied to both surfaces. The dielectric constant was then measured at a frequency of 1 kHz using an Agilent 4294A precision impedance analyzer (USA). The optical properties of the samples were investigated by ultraviolet-visible diffuse reflectance spectroscopy (UV–vis DRS) using a spectrophotometer (UV-3600i Plus, Shimadzu, Japan) over the wavelength range of 200–800 nm. E_g was determined from the Tauc plot by extrapolating the linear region of the $(\alpha h\nu)^2$ versus $h\nu$ plot to the energy axis ($h\nu$).

2.4 Electrochemical measurements

The working electrode was prepared by homogeneously mixing 10 mg of piezocatalyst with 20 μL ethanol and 20 μL Nafion solution to form a paste, which was then uniformly coated onto a 1 cm^2 active area of ITO glass. Electrochemical measurements were conducted in a three-electrode system using the prepared electrode as the working electrode, a Pt mesh (2 cm × 2 cm) as the counter electrode, and a saturated calomel electrode (SCE) as the reference. The electrolyte was a 0.5 M Na_2SO_4 aqueous solution. Mott–Schottky plots were measured at a fixed frequency of 500 Hz and an AC amplitude of 5 mV. Electrochemical impedance spectroscopy (EIS) was recorded from 0.1 Hz to 100 kHz with an AC amplitude of 5 mV at a bias voltage of 1.2 V. All tests were performed on an electrochemical workstation (CHI660E, CH Instruments, China).

2.5 Piezocatalytic hydrogen production

The piezocatalytic hydrogen production experiment was conducted as follows. First, 20 mg of the piezocatalysts was dispersed in 15 mL of a mixed solution containing deionized water and methanol (MeOH) (9 : 1, *v*/*v*). For comparison, the experiments were conducted using 10 vol% triethanolamine (TEOA), 0.1 M sodium sulfite (Na_2SO_3), or 0.1 M ethylenediaminetetraacetic acid (EDTA) as the sacrificial agent. The suspension was sealed in a glass bottle after purging with argon for 10 min to remove dissolved air. The sealed reactor was then placed in an ultrasonic cleaner (KQ-100VDV, China) and subjected to vibration (100 W, 45 kHz) in the dark at a controlled temperature of ~30 °C. To evaluate the catalytic performance, 1 mL of headspace gas was sampled with a syringe and analyzed using a gas chromatograph (GC-7820, Agilent, USA) to quantify the produced H_2. The amount of H_2 was calculated from its peak area based on a calibration curve from standard gas. Each experiment was repeated multiple times to ensure data reliability.

2.6 Piezocatalytic degradation of organic pollutants

The piezocatalytic activity of the BWO samples was evaluated by the degradation of Rhodamine B (RhB) in an aqueous solution. In a typical experiment, a specified dosage of catalyst (10, 25, or 50 mg) was dispersed in 50 mL of RhB solution (10 mg·L^{-1}). To establish adsorption–desorption equilibrium, the suspension was magnetically stirred in the dark for 30 min. Subsequently, the reactor was placed in an ultrasonic cleaner (KQ-100VDV, Kunshan Ultrasonic Instruments Co., Ltd., China) at 100 W and 45 kHz to initiate the catalytic reaction. 3 mL aliquots of the suspension were withdrawn every 5 min and centrifuged to separate the catalyst, and the resulting supernatant was analyzed for its absorbance at ~555 nm using a spectrophotometer (UV-2450, Shimadzu, Japan) with deionized water as the reference. Each experiment was repeated multiple times to ensure data reliability.

3 Results and discussion

3.1 Structural and morphological analysis

Figure 1(a) displays the XRD patterns of BWO samples synthesized with varying surfactant contents. All samples exhibit characteristic diffraction peaks at 28.24°, 32.88°, 47.12°, 55.82°, 58.42°, 68.90°, 76.02°, and 78.34°, which correspond to the (131), (200), (202), (133), (262), (004), (333), and (460) crystallographic planes of orthorhombic-phase BWO (PDF#79-2381), respectively, as supported by prior studies [25]. Notably, no impurity peaks are detected. The introduction of CTAB results in significant attenuation and broadening of the main diffraction peaks, a phenomenon primarily attributed to reduced crystallinity and grain refinement [31]. XRD characterizes the long-range ordered structure of the crystalline bulk phase, while the bonding between surface dangling bonds on BWO and Br^- ions from CTAB is confined to the top few atomic layers. Consequently, this surface interaction exerts no detectable influence on the bulk lattice, and thus, no shift in XRD peak positions is observed (Fig. 1(b)). SEM micrographs reveal that while both BWO samples form fluffy, sheet-like aggregates, CTAB-modified BWO exhibits a significantly more uniform and flatter ultrathin nanosheet morphology than pristine BWO (Figs. 1(c) and 1(d)). This distinct contrast underscores the pivotal role of CTAB as a structure-directing agent, which governs nanosheet growth to yield well-defined nanostructures. The corresponding EDS elemental mapping analysis confirms the homogeneous distribution of Bi, W, O, and Br across the CTAB-modified BWO nanosheets (Figs. 1(e)–1(h)). The detection of Br confirms that CTAB was successfully incorporated into the BWO samples during synthesis and was uniformly distributed throughout the nanosheets. The successful incorporation of Br into BWO was also confirmed by ICP-MS (Fig. 1(i) and Table S2 in the ESM). As shown in Fig. 1(j), TEM characterization reveals a nearly transparent, two-dimensional, planar ultrathin nanosheet morphology for CTAB-modified BWO. The HRTEM image further displays distinct lattice fringes with a *d*-spacing of 0.32 nm, indexed to the (131)

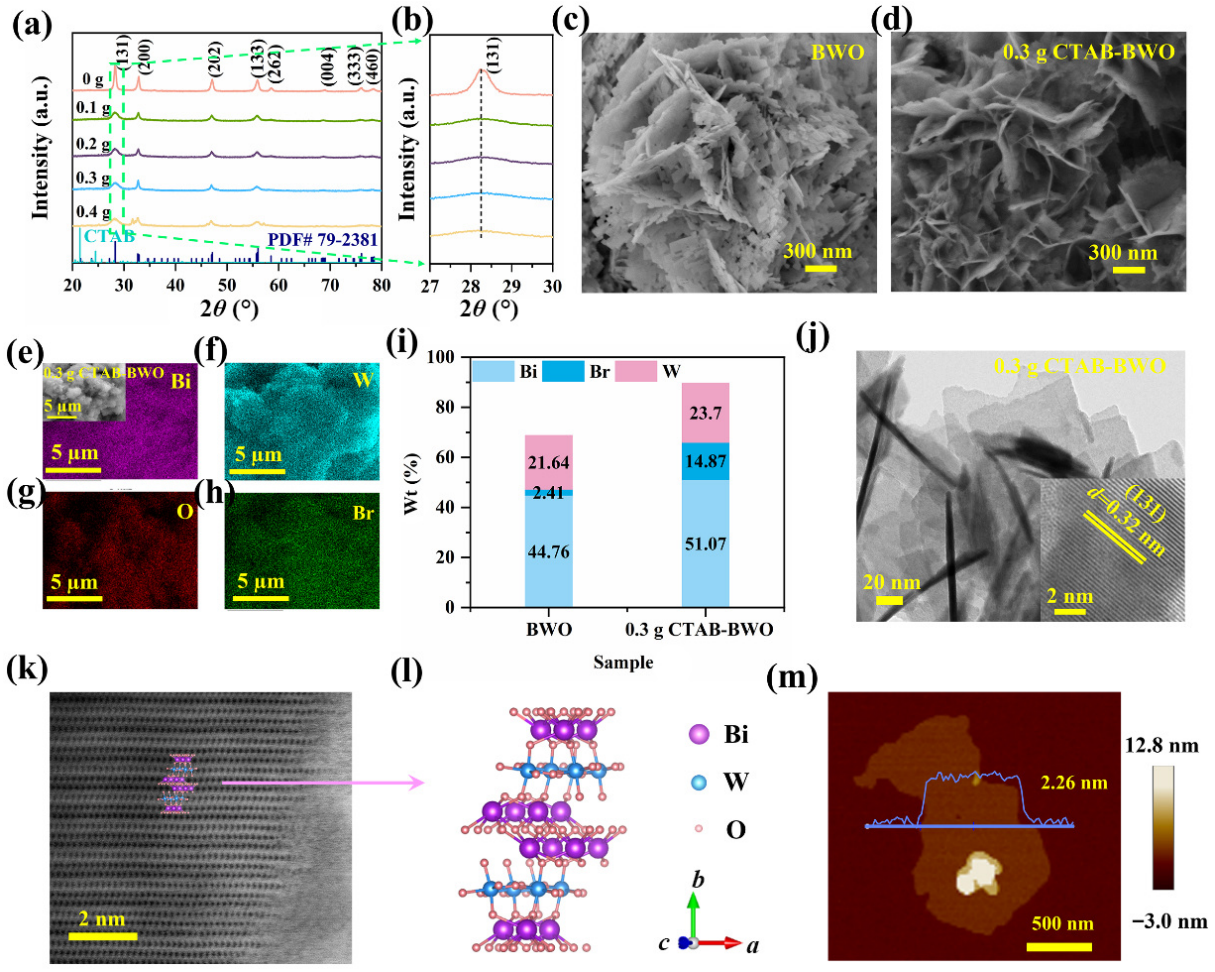

Fig. 1 (a) X-ray diffraction (XRD) patterns and (b) partially enlarged XRD patterns. (c, d) Scanning electron microscopy (SEM) images of BWO before and after CTAB modification. (e–h) Energy-dispersive X-ray spectrometer (EDS) elemental mapping analysis of Bi, W, O, and Br. The inset is the corresponding SEM image. (i) Elemental contents in BWO before and after CTAB modification, as determined by inductively coupled plasma spectrometry/mass spectrometry (ICP-MS). (j) High-resolution transmission electron microscopy (HRTEM) images. (k) Aberration-corrected scanning transmission electron microscopy (STEM) image of BWO after CTAB modification. The inset image denotes the structure model. (l) Enlarged view of the structure model. (m) Atomic force microscopy (AFM) and the corresponding thickness of CTAB-modified BWO.

plane of orthorhombic BWO, confirming the preservation of crystalline integrity after modification (the inset of Fig. 1(j)). The aberration-corrected HAADF-STEM image of the CTAB-modified BWO sample is displayed in Fig. 1(k). In this image, the dark gray spots correspond to the Bi atomic columns (Z = 83, where Z is the atomic number), while the light gray spots represent the W columns (Z = 74). Notably, Br atoms are not detected in the STEM image. This observation confirms that because bonding occurs on the surface, Br neither substitutes for any atoms in the BWO lattice nor resides in interstitial sites. The corresponding structure model, shown in the inset of Fig. 1(k), aligns well with the observed STEM image, and a magnified version of this model is provided in Fig. 1(l). AFM images and corresponding height profiles reveal that the CTAB-modified BWO nanosheets have a minimum thickness of approximately 2.26 nm (Fig. 1(m)). The thinner structure can shorten the charge migration distance from the bulk phase to the surface, thereby effectively reducing the recombination rate.

The surface elemental composition and electronic states of the prepared samples were analyzed by XPS spectroscopy (Figs. 2(a)–2(e)). Apart from the characteristic peaks corresponding to Bi, W, O, C, and Br, no additional elemental peaks are observed (Fig. 2(a)). Compared to BWO without CTAB modification, nearly all elemental peaks of CTAB-modified BWO exhibit shifts toward lower binding energies (Figs. 2(b)–2(d)). A decrease in XPS binding energy typically indicates an increase in the electron cloud density of the outer atomic orbitals of the material. This phenomenon suggests weakened nuclear attraction to the outermost electrons, thereby facilitating electron participation in catalytic reactions [32]. For semiconductor materials, lowered XPS binding energy modifies their band structure. Specifically, the downward shift in binding energy induces an upward displacement of the valence band maximum in BWO materials, thereby altering their E_g. This conclusion is further corroborated by subsequent UV-vis DRS characterization analyses. To confirm the presence of Br in CTAB-modified BWO nanosheets, the Br 3d XPS spectra of BWO are presented in Fig. 2(e). The modified sample exhibits a distinct Br 3d signal within a specific energy range, featuring a prominent peak centered at ~67.2 eV. Conversely, this characteristic peak is absent in pristine BWO. The presence of such a strong Br 3d peak indicates that Br^- ions from CTAB are bonded to the surface Bi atoms of the Bi_2WO_6 nanosheets [29]. To enhance catalytic activity, increasing the surface area of the materials is a well-established strategy for providing more active sites. Accordingly, N_2 adsorption–desorption isotherms were measured to evaluate the

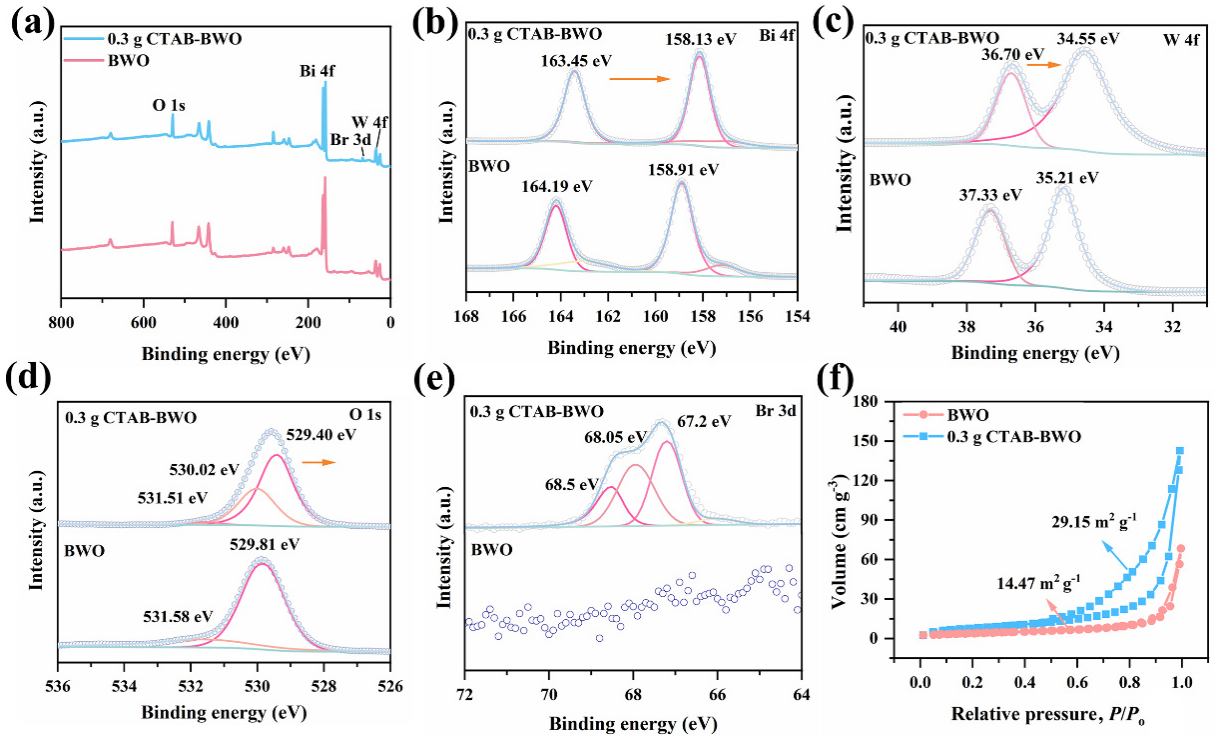

Fig. 2 (a) X-ray photoelectron spectroscopy (XPS) survey spectra of BWO before and after CTAB modification. High-resolution XPS spectra of (b) Bi 4f, (c) W 4f, (d) O 1s, and (e) Br 3d. (f) S_{BET} analysis of BWO before and after CTAB modification.

effect of CTAB modification. As shown in Fig. 2(f), the S_{BET} of the CTAB-modified BWO (29.15 $m^2 \cdot g^{-1}$) is more than twice that of the pristine BWO (14.47 $m^2 \cdot g^{-1}$). This significant increase in S_{BET} likely contributes to the enhanced piezocatalytic activity by exposing more active sites and providing greater interfaces for charge-reactant interactions.

3.2 Piezoelectric performance

As piezoelectric performance is a critical determinant of piezocatalytic activity, PFM was conducted to assess the effect of CTAB modification. In the amplitude image (Fig. 3(a)) and phase image (Fig. 3(d)) of PFM, pristine BWO exhibits distinct amplitude contrast and phase variation, with a corresponding average amplitude value of ~50 pm (Fig. 3(c)). Notably, CTAB-modified BWO nanosheets demonstrate a higher contrast of amplitude (Fig. 3(b)) and phase image (Fig. 3(e)), with a corresponding average amplitude value of ~130 pm (Fig. 3(c)). The phase angle distribution curve of pristine BWO is between −80° and 100°, while that of CTAB-modified BWO nanosheets is more convergent from −50° to 50° (Fig. 3(f)). A narrower phase distribution indicates a higher degree of orientation of the local polarization direction [33–35]. The local piezoelectric hysteresis loops of BWO before and after CTAB modification are shown in Figs. 3(g) and 3(h). Both phase angles in the local hysteresis loop exhibit an ~170° change under the reversal of the 10 V DC bias field, which confirms the piezoelectric response of BWO. As presented in the typical amplitude-voltage butterfly loops, the maximum amplitudes of BWO before and after CTAB modification are 443.13 and 725.03 pm, respectively (Figs. 3(g) and 3(h)). As shown in the PFM amplitude curves in Fig. 3(i), the effective piezoelectric coefficient (d^*_{33}) values of BWO before and after CTAB modification are calculated as ~10.01 and ~27.53 pm·V^{-1}, respectively. These findings demonstrate that CTAB modification substantially optimizes the piezoelectric properties.

To elucidate the mechanism behind the CTAB-induced piezoelectric enhancement in BWO, KPFM was employed to measure the contact potential difference (CPD). The CTAB-modified BWO exhibited a CPD approximately 18.34 mV higher than that of the pristine sample (Figs. 4(a)–4(c)), a result indicative of greater free space charge adsorption [36–38]. Reducing the material thickness increases the relative volume of the interface layer, making interfacial polarization dominant. Additionally, Br^- ions from CTAB form a passivation layer, which increases the dielectric constant from 32.60 to 37.76 for BWO before and after CTAB modification (Fig. S2 in the ESM) [39,40]. Thinner materials also promote a nonuniform space charge distribution, which enhances the local internal electric field. This built-in field lowers the energy barrier for domain inversion, facilitating polarization reversal and significantly boosting the piezoelectric coefficient [41–44].

To evaluate the impact of CTAB modification on carrier separation and transfer efficiency, Mott–Schottky curves and EIS of BWO before and after CTAB modification were investigated (Figs. 4(d)–4(i)). The carrier concentration (N_d) was determined from Eq. (1) [8]:

$$N_d = \left(\frac{2}{e_0 \varepsilon_0 \varepsilon}\right)\left(d\frac{(1/C^2)}{dV}\right)^{-1} \quad (1)$$

where e_0, ε_0, ε, C, and V correspond to the electronic charge unit, vacuum permittivity, dielectric constant of the material, capacitance, and voltage, respectively. Thus, the N_d values for the materials under both vibrational and nonvibrational conditions were calculated. The application of ultrasonic mechanical vibration provides a driving force that enhances piezoelectric charge separation and initiates the piezocatalytic reaction. The N_d of the pristine BWO without any vibration is $N_d \approx 4.31\times10^{20}$ cm^3. After CTAB modification, the N_d of CTAB-modified BWO increases to $N_d \approx 8.17\times10^{20}$ cm^3. CTAB acts as a morphology-controlling agent, using selective adsorption to suppress the

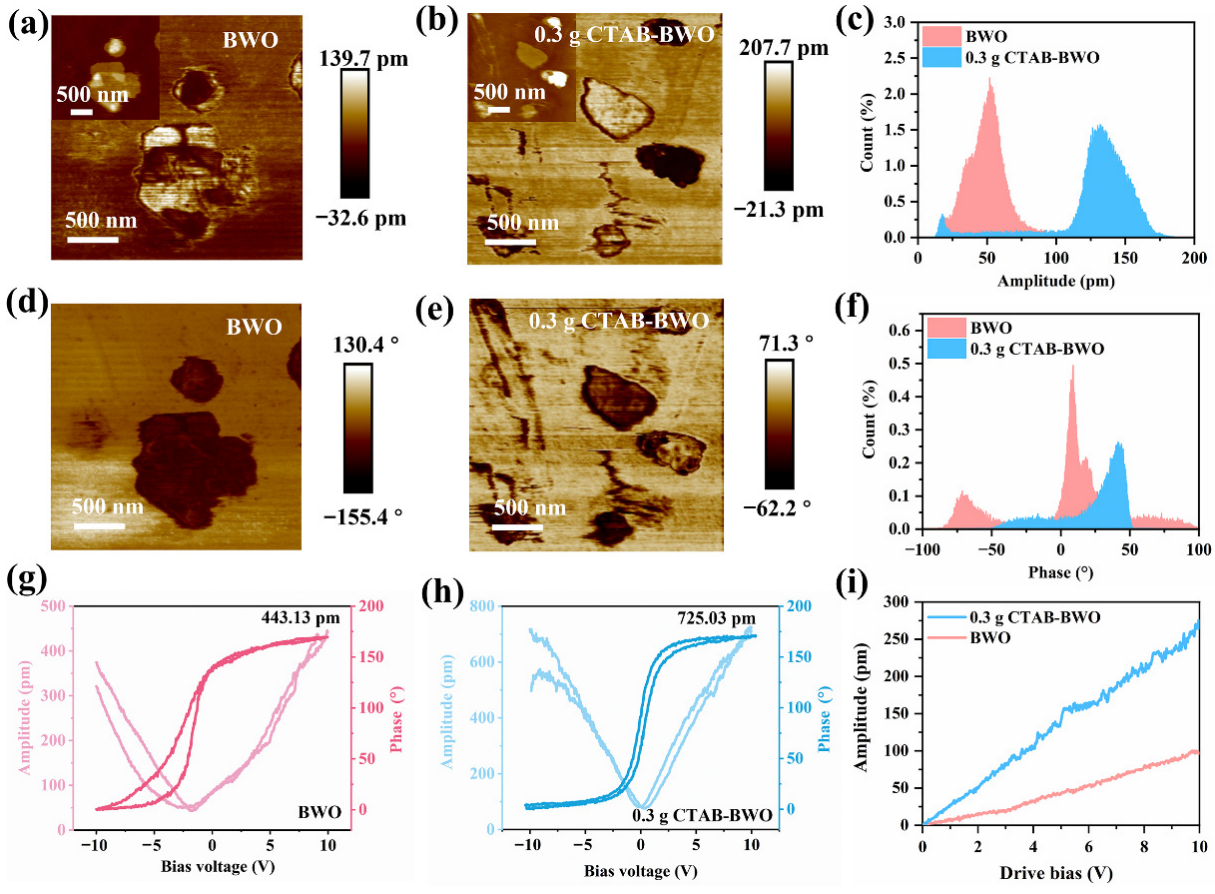

Fig. 3 (a, b) Piezoresponse force microscopy (PFM) amplitude images. The insets are the corresponding AFM images. (c) Amplitude distribution histogram. (d, e) PFM phase images. (f) Phase angle distribution histogram. (g, h) Local piezoelectric hysteresis loops and (i) PFM amplitude curves of BWO before and after CTAB modification.

growth in thickness and form a two-dimensional structure of BWO. This ultrathin architecture shortens the carrier migration distance, effectively inhibiting bulk recombination and leading to a higher N_d. When subjected to ultrasonic vibrations, the N_d of both materials increases significantly. Specifically, the N_d values for pristine BWO and CTAB-modified BWO increase to $N_d \approx 5.22\times10^{20}$ cm^3 and $N_d \approx 9.70\times10^{20}$ cm^3, respectively, representing a 1.86-fold increase (Fig. 4(f)). Moreover, the changes in carrier concentration induced by vibration ($\Delta N_d = N_d$ (with vibration) − N_d (without vibration)) are quantified as 0.91×10^{20} cm^{-3} for pristine BWO and 1.53×10^{20} cm^{-3} for the modified sample (Fig. 4(g)). The large ΔN_d value for CTAB-modified BWO indicates that its enhanced piezoelectric response leads to a greater generation of carriers upon vibrational stimulation compared to pristine BWO. This increase in carrier concentration directly contributes to the probability of redox reactions, thereby amplifying the effect of the improved piezoelectric coefficient.

The above results can be further confirmed by EIS measurements with or without ultrasonic vibration. The semicircular arcs in the Nyquist plots reflect the charge transfer kinetics at the electrode interface [45]. As shown in Figs. 4(h) and 4(i), CTAB-modified BWO exhibits a smaller impedance arc radius than pristine BWO, which corresponds to a lower interfacial resistance and higher charge transfer efficiency. When exposed to ultrasonic vibrations, the impedance arc radius of both materials is reduced, indicating that their charge transfer efficiency has been further enhanced. Notably, CTAB-modified BWO exhibits a more significant reduction in the impedance arc radius, indicating that the built-in electric field generated by piezoelectric polarization serves as the dominant mechanism responsible for the significant reduction in charge transfer impedance under ultrasonic conditions, whereas the contribution of mechanical vibration to mass transfer enhancement is relatively secondary [46].

3.3 Piezocatalytic activity and mechanism

In piezocatalytic water splitting, the efficiency of hydrogen evolution is often limited by charge recombination. Hole sacrificial agents, such as MeOH [26], TEOA [25], EDTA [47], Na_2S and Na_2SO_3 [48], are used to consume positive charges and enhance efficiency. For comparison, the experiments were conducted using TEOA, Na_2SO_3, or EDTA as the sacrificial agent (Fig. 5(a)). The results show that MeOH yields the highest average hydrogen evolution efficiency, followed by Na_2SO_3, while EDTA and TEOA exhibit comparable, lower performance. To investigate the effect of CTAB content on the piezocatalytic performance of BWO for water splitting, we tested samples with 0–0.4 g of CTAB (Fig. 5(b)). The average piezocatalytic hydrogen production rate initially increases with the addition of CTAB from 54.24 μmol·g^{-1}·h^{-1} for the pristine BWO to 553.50 μmol·g^{-1}·h^{-1} for the 0.3 g CTAB-modified BWO, which is an enhancement of ~10.2 times. The piezocatalytic activity is not solely determined by the piezoelectric coefficient but is jointly governed by factors such as carrier concentration, carrier separation efficiency, and specific surface area [10,49]. In addition, further increasing the CTAB amount led to a decline in performance, likely due to excessive CTAB accumulation on the catalyst surface, which blocked active reaction sites [50]. To optimize the piezocatalytic hydrogen

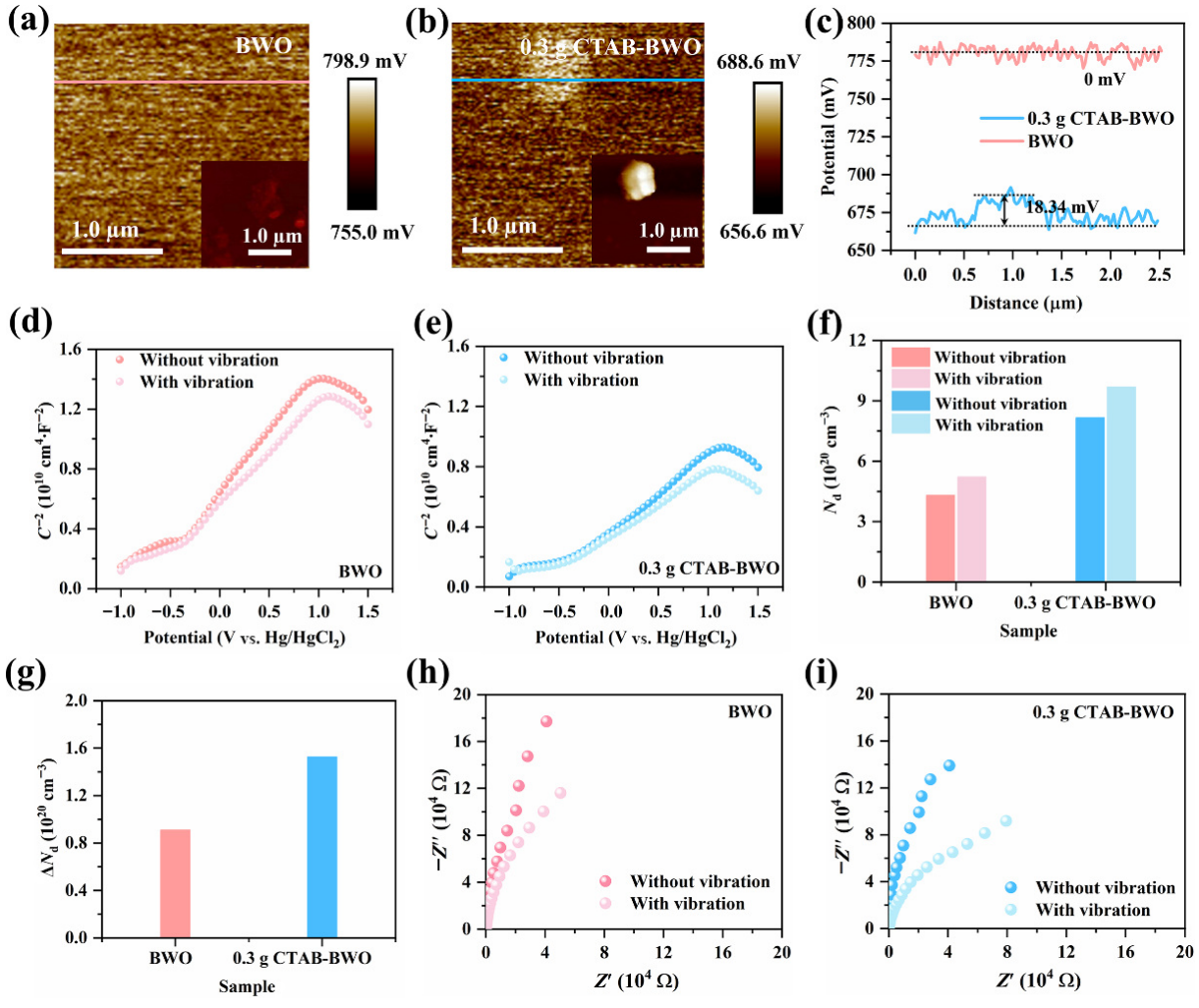

Fig. 4 (a, b) Surface contact potential difference (CPD) of BWO before and after CTAB modification. The insets are the corresponding AFM images. (c) Surface CPD along the lines in (a, b). (d, e) Mott–Schottky curves, (f) calculated carrier concentration (N_d), and (g) ΔN_d with/without vibration of BWO. Electrochemical impedance spectroscopy (EIS) Nyquist curves of (h) BWO and (i) 0.3 g CTAB-BWO with/without vibration.

evolution performance, both pristine and CTAB-modified BWO samples were subjected to ultrasonic treatment in suspension (see experimental schematic in Fig. S3 in the ESM). The hydrogen production rates exhibit a near-linear relationship with the vibration time (Fig. 5(c)). Notably, CTAB-modified BWO achieved an average rate of 6120.31 μmol·g^{-1}·h^{-1}, a significant improvement over the 4049.72 μmol·g^{-1}·h^{-1} for unmodified BWO (Fig. 5(d)). Ultrasonic irradiation generates intense cavitation effects and microjets in the liquid suspension. This physical force helps to effectively exfoliate the catalyst agglomerates and improve the dispersion of the nanosheets. Consequently, this leads to increased effective surface area utilization and shortened reactant diffusion paths, thereby jointly optimizing the interfacial charge transfer kinetics and enhancing the hydrogen evolution rate [45]. The per-unit-power hydrogen production rate reaches 61.20 μmol g^{-1}·h^{-1}·W^{-1}, representing one of the highest values reported to date (Fig. 5(e) and Table S3 in the ESM).

The enhancement of the piezocatalytic performance of BWO mediated by CTAB was further reflected in the degradation efficiency of the RhB dye solution. The piezocatalytic degradation of RhB is significantly enhanced by CTAB modification. After a 30-min dark adsorption period, CTAB-modified BWO achieved 89.77% degradation, far surpassing the 20.02% for pristine BWO, representing an overall performance improvement of ~4.5 times (Figs. S4(a)–S4(c) in the ESM). This is attributed to the Br-modified structure promoting stronger RhB^+ adsorption and the larger surface area and enhanced piezoelectricity of the nanosheets, which provide more active sites and improve charge separation. The catalyst dosage was also optimized, with 25 mg identified as the ideal amount. Higher dosages (e.g., 50 mg) reduce efficiency due to particle aggregation, which decreases the surface area and blocks active sites (Figs. S5(a)–S5(d) in the ESM).

Mott–Schottky analysis was used to determine the flat-band potential (E_f) of the materials (Figs. 4(d) and 4(e)). Both the pristine and CTAB-modified BWO exhibit a flat-band potential of −0.85 V vs. SCE. After converting to the reversible hydrogen electrode (RHE) scale using Eq. (2) (pH = 6.8) [45]:

$$E_{f,\mathrm{RHE}} = E_{f,\mathrm{SCE}} + (0.0591 \times \mathrm{pH} + 0.24)\ \mathrm{V} \quad (2)$$

The $E_{f\text{RHE}}$ for both samples are calculated to be −0.21 V. The positive slopes of the curves confirm the n-type semiconducting nature of BWO. For n-type semiconductors, the conduction band (CB) minimum is typically ~0.3 V more negative than the flat-band potential [26,51]. Accordingly, the CB potential for both samples was determined to be −0.51 V vs. RHE. Figure 5(f) displays the UV–vis DRS spectra of BWO nanosheets with and without CTAB modification. No significant differences are observed between the spectra of BWO nanosheets with varying thicknesses. The corresponding E_g determined from Tauc plots, is

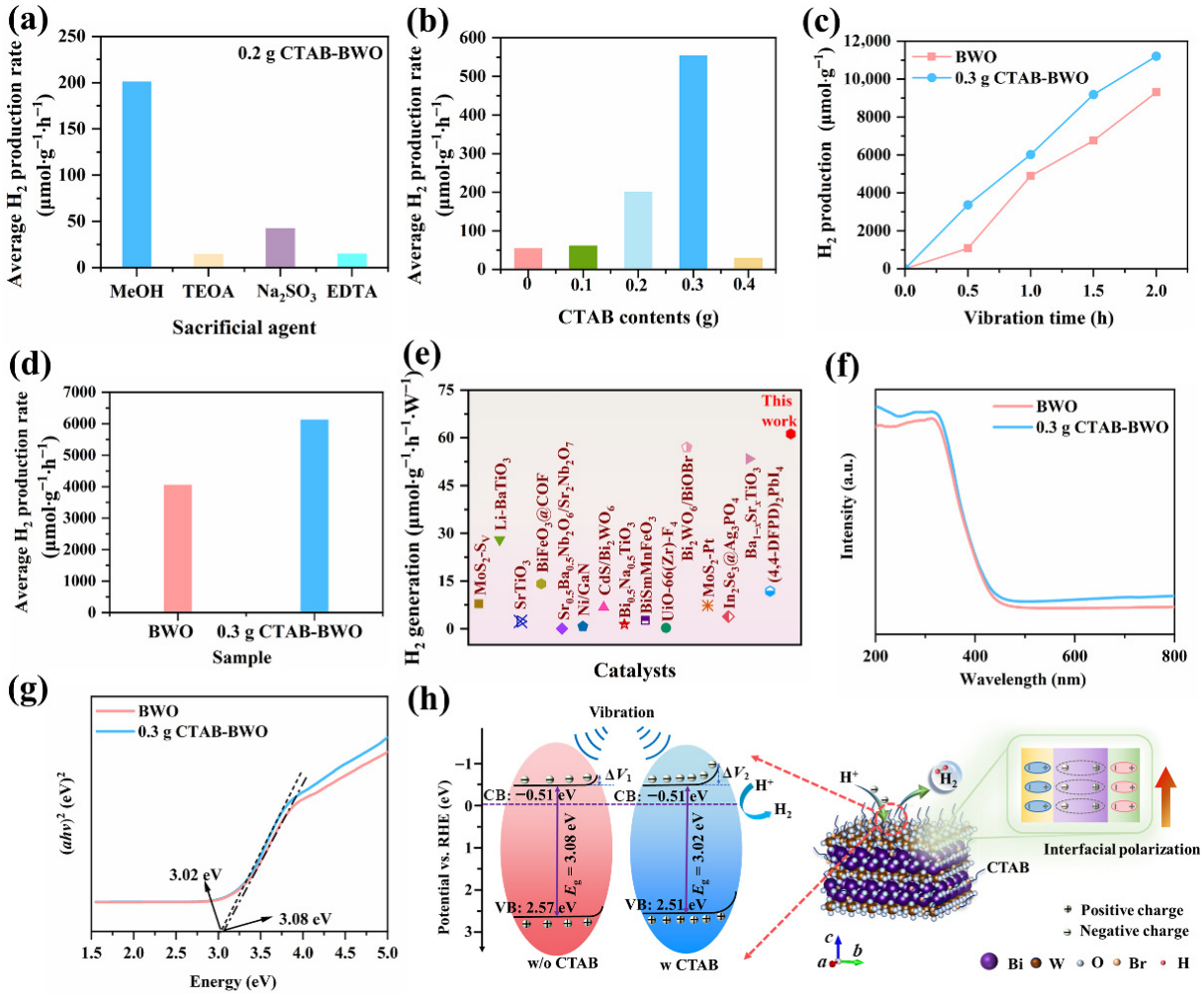

Fig. 5 Piezocatalytic hydrogen evolution rates (a) under different sacrificial agents and (b) after different masses of CTAB modification and (c) piezocatalytic hydrogen production under different vibration times and (d) average hydrogen production rate in suspension. (e) Comparison of the piezocatalytic hydrogen production efficiency of different catalysts. (f) UV–vis spectra, (g) Tauc plots, and (h) mechanism diagram of piezocatalytic hydrogen evolution of BWO.

3.08 eV for pristine BWO and 3.02 eV for CTAB-modified BWO (Fig. 5(g)). This bandgap narrowing is attributed to an upward shift in the valence band maximum induced by Br^- surface modification [29,31]. The reversible hydrogen electrode (RHE, pH = 6.8) for H^+/H_2 (pH = 7.0) is approximately −0.01 V, confirming the thermodynamic feasibility for hydrogen evolution. By combining the CB level and E_g, the valence band (VB) potentials of BWO and CTAB-modified BWO are calculated to be 2.57 and 2.51 V, respectively.

The mechanism diagram of piezocatalytic hydrogen evolution of CTAB-modified BWO is shown in Fig. 5(h). The activation of the piezoelectric effect and polarization fields induces significant band bending through the redistribution of electronic potentials [52]. CTAB modification optimizes the interfacial polarization of BWO, which further enhances its piezoelectric response. This results in a greater degree of band tilting ($\Delta V_2 > \Delta V_1$), creating a stronger built-in electric field and thus a more powerful driving force for charge separation [53]. Under ultrasonic vibration, the piezoelectric effect induces a dynamic polarization within the material, generating separated positive charges (q^+) and negative charges (q^-) on opposite surfaces (Reaction (3)):

$$\text{wCTAB-BWO} \xrightarrow{\text{Vibration}} \text{wCTAB-BWO} + q^+ + q^- \quad (3)$$

Driven by the resulting built-in electric field, these piezo-induced charges migrate to participate in redox reactions. Here, MeOH serves as a hole scavenger, consuming the positive charges (q^+) to produce protons (H^+) and hydroxymethyl radical intermediates ($\cdot CH_2OH$). Concurrently, the negative charges (q^-) reduce these protons at the active sites, ultimately forming H_2 (Reaction (4)):

$$2H^+ + 2q^- \rightarrow H_2 \quad (4)$$

Energy band theory draws on the mature photocatalytic system, in which the energy band structure and electronic state of the piezocatalyst are the key factors determining the piezocatalytic activity [52]. Unlike band theory, the mechanism of the screening charge effect highlights the dominant role of the piezoelectric potential and its associated surface screening behavior in piezoelectric materials [54]. While both the energy band theory and the screening charge theory offer plausible explanations for various piezocatalytic processes based on their respective experimental observations, the precise reaction mechanism remains a subject of debate. A limitation of the energy band theory is that not all piezoelectric materials possess an appropriate energy band structure conducive to catalysis. Regarding the screening charge theory, it is argued that electrons accumulated on the surface of piezoelectric materials via the piezoelectric effect may not spontaneously participate in catalytic reactions [55].

Overall, these mechanisms clarify the complex interactions that affect the efficiency of piezocatalytic reactions.

As a ferro-/pyroelectric material, BWO has been successfully applied in pyro-catalytic carbon dioxide reduction by harvesting cold–hot alternation energy (15–70 °C), achieving a final methanol yield of 55.0 μmol·g^{-1} after 20 thermal cycles with heating and cooling rates of 11 °C min^{-1} [56]. To isolate the piezocatalytic effect, the reaction temperature was monitored. As shown in Fig. S6 in the ESM, even without active cooling, the bulk solution temperature gradually increases from 30 °C to only 35 °C within 12.5 min, corresponding to a heating rate of merely 0.4 °C·min^{-1}. Given the minimal temperature fluctuation (ΔT) and slow rate of change (dT/dt), the pyroelectric effect is insufficient to generate a detectable pyro-current or significant catalytic yield [49]. Since piezocatalysis is exerted through ultrasonic vibration, friction and bending forces are inevitable. Among them, flexoelectricity induces polarization via strain gradients to drive catalysis, extending mechanocatalysis beyond piezoelectric materials [10,57–59]. Tribocatalysis utilizes friction-generated charges and interfaces to accelerate reactions and applies to a wide range of materials [60–65]. Since the catalyst we used was a piezoelectric material with an asymmetric center, we attribute the primary catalytic effect to the piezoelectric effect.

4 Conclusions

In this work, two-dimensional ultrathin BWO nanosheets with a minimal thickness of ~2.26 nm were controllably synthesized using CTAB-assisted hydrothermal synthesis, and their piezocatalytic properties were analyzed. The specific surface area more than doubled, increasing from 14.47 to 29.15 m^2·g^{-1}, and the interfacial polarization was significantly enhanced by 18.34 mV. Consequently, the effective piezoelectric coefficient of CTAB-modified BWO rose from ~10.01 to ~27.53 pm·V^{-1}. The CTAB-modified BWO, by simultaneously increasing reactive sites and boosting piezoelectric performance, achieves a maximum per-unit-power hydrogen production rate of 61.20 μmol·g^{-1}·h^{-1}·W^{-1}, which is one of the highest values ever reported. This work demonstrates a synergistic strategy of morphology engineering to enhance the surface reactivity and piezoelectric response, offering a new paradigm for high-performance piezocatalysts.

Acknowledgements

This work is financially supported by the National Natural Science Foundation of China (Nos. 22309170 and 22179108), the Natural Science Foundation of Zhejiang Province (Nos. LQ24E020003, LQN25E020017, and LD25B060001), the Open Fund Project of the National-Local Joint Engineering Research Center of Heavy Metals Pollutants Control and Resource Utilization of Nanchang Hangkong University (No. ES202480182), and the Fundamental Research Funds for the Provincial Universities of Zhejiang (Nos. 2024YW14 and 2025QN065). The authors extend their gratitude to Mr. Deyou Chen and Ms. Jiawen Sun (from Scientific Compass www.shiyanjia.com) for providing invaluable assistance with the dielectric constants and ICP-MS tests.

Author contributions

Xiaoli Xu: Conceptualization, supervision, writing – review & editing and funding acquisition. Ying Wang: Prepared the samples and carried out experiments, Writing – Original Draft. Wanwan Cheng: Prepared the samples and characterization, Data curation. Huan Zhai: Data curation. Jinqian Ma: Data curation. Lingbo Xiao: supervision, writing – review & editing and funding acquisition. Laishun Qin: supervision, writing – review & editing. Wenwen Liu: Data curation. Yanmin Jia: Writing – review & editing. Zhenhai Wen: writing – review & editing. Da Chen: Supervision, Writing – Review & Editing and Funding acquisition.

Availability of data and materials

The data that support the findings of this study are available from the corresponding author upon reasonable request.

Competing interests

The authors have no competing interests to declare that are relevant to the content of this article.

Electronic Supplementary Material

Supplementary material is available in the online version of this article at https://doi.org/10.26599/JAC.2026.9221255.

References

[1] Peng ZM, Zhang Q, Qi GC, *et al.* Nanostructured Pt@RuO catalyst for boosting overall acidic seawater splitting. *Chin J Struct Chem* 2024, **43**: 100191.

[2] Wu H, Zhang Q, Liu QF, *et al.* Research on NiFe-based oxygen evolution reaction catalysts and application in electrolytic seawater hydrogen production. *J Funct Mater Devices* 2024, **30**: 225–232. (in Chinese)

[3] Kubota K, Pang YD, Miura A, *et al.* Redox reactions of small organic molecules using ball milling and piezoelectric materials. *Science* 2019, **366**: 1500–1504.

[4] Wu JY, Meng Y, Wu F, *et al.* Ultrasound-driven non-metallic Fenton-active center construction for extensive chemodynamic therapy. *Adv Mater* 2024, **36**: 2307980.

[5] Xia TT, Lu LZ, Zhang HY, *et al.* Inducing piezoelectricity in distorted rutile TiO_2 for enhanced tetracycline hydrochloride degradation through photopiezocatalysis. *J Adv Ceram* 2024, **13**: 323–331.

[6] Li LT, Wang C, Huang CR, *et al.* Recyclable molecular ferroelectrics to harvest mechanical energy for sustained hydrogen generation. *J Am Chem Soc* 2025, **147**: 12635–12643.

[7] Liu LZ, Huang HW, Chen ZS, *et al.* Synergistic polarization engineering on bulk and surface for boosting CO_2 photoreduction. *Angew Chem Int Ed* 2021, **60**: 18303–18308.

[8] Hu C, Chen F, Wang YG, *et al.* Exceptional cocatalyst-free photo-enhanced piezocatalytic hydrogen evolution of carbon nitride nanosheets from strong in-plane polarization. *Adv Mater* 2021, **33**: 2101751.

[9] Yu HJ, Wei XD, Wang M, *et al.* Macroscopic polarization enhancement boosting piezo-photocatalytic performance via Nb-doping on B-site of $Bi_4Ti_3O_{12}$ nanosheets. *J Adv Ceram* 2024, **13**: 437–446.

[10] Xu XL, Wang Y, Cheng WW, *et al.* Recent advances in piezocatalytic hydrogen production and prospects. *Surf Interfaces* 2024, **54**: 105245.

[11] Wu JM, Sun YG, Chang WE, *et al.* Piezoelectricity induced water splitting and formation of hydroxyl radical from active edge sites of MoS_2 nanoflowers. *Nano Energy* 2018, **46**: 372–382

[12] Xue KL, Jiang Y, Mofarah SS, *et al.* Composition-driven morphological evolution of $BaTiO_3$ nanowires for efficient piezocatalytic hydrogen production. *Chemosphere* 2023, **338**: 139337.

[13] Liu DM, Jin CC, Shan FK, *et al.* Synthesizing $BaTiO_3$ nanostructures to explore morphological influence, kinetics, and mechanism of piezocatalytic dye degradation. *ACS Appl Mater Int* 2020, **12**: 17443–17451.

[14] Zhao JJ, Guo TY, Wang HT, *et al.* BiOBr nanoflakes with engineered thickness for boosted photodegradation of RhB under visible light irradiation. *J Alloys Compd* 2023, **947**: 169613.

[15] Abbood HA, Alabadi A, Al-Hawash AB, *et al.* Square CdS micro/

nanosheets as efficient photo/piezo-bi-catalyst for hydrogen production. *Catal Lett* 2020, **150**: 3059–3070.
[16] Xiao LB, Xu XL, Wu Z, *et al.* Recent progress and prospect of friction-driven-tribocatalysis: From basic principle to material design. *Surf Interfaces* 2025, **56**: 105557.
[17] Mo Y, Wu JY, Liu W, *et al.* Ultrafast piezocatalytic organic pollutant degradation enabled by dynamic spin state regulation of cobalt in nano-ferroelectrics. *Adv Powder Mater* 2025, **4**: 100307.
[18] Feng WH, Yuan J, Zhang LL, *et al.* Atomically thin ZnS nanosheets: Facile synthesis and superior piezocatalytic H_2 production from pure H_2O. *Appl Catal B Environ* 2020, **277**: 119250.
[19] Su R, Zhang JH, Wong V, *et al.* Engineering sub-nanometer hafnia-based ferroelectrics to break the scaling relation for high-efficiency piezocatalytic water splitting. *Adv Mater* 2023, **35**: 2303018.
[20] He YW, Tian N, An Y, *et al.* Morphology regulation and oxygen vacancy construction synergistically boosting the piezocatalytic degradation and pure water splitting of $SrTiO_3$. *Small* 2024, **20**: 2407624.
[21] Wang K, Shu Z, Zhou J, *et al.* Enhancing piezocatalytic H_2O_2 production through morphology control of graphitic carbon nitride. *J Colloid Interf Sci* 2023, **648**: 242–250.
[22] Li MT, Zhou JH, Di R, *et al.* Piezoelectric potential activated interfacial electric field in $BiFeO_3$@$BaTiO_3$ heterojunction for rapid and round-the-clock photocatalytic degradation of organic pollutants. *J Adv Ceram* 2024, **13**: 2030–2042.
[23] Li S, Zhao ZC, Li JB, *et al.* Mechanically induced highly efficient hydrogen evolution from water over piezoelectric SnSe nanosheets. *Small* 2022, **18**: 2202507.
[24] Wang JJ, Hu C, Zhang YH, *et al.* Engineering piezoelectricity and strain sensitivity in CdS to promote piezocatalytic hydrogen evolution. *Chin J Catal* 2022, **43**: 1277–1285.
[25] Xu XL, Xiao LB, Wu Z, *et al.* Harvesting vibration energy to piezo-catalytically generate hydrogen through Bi_2WO_6 layered-perovskite. *Nano Energy* 2020, **78**: 105351.
[26] Wang Y, Xu XL, Xiao LB, *et al.* Balancing the piezoelectric coefficient and carrier concentration of Bi_2WO_{6-x} for ultrahigh piezocatalysis. *J Adv Ceram* 2024, **13**: 1737–1747.
[27] Ning XE, Hao AZ, Cao YL, *et al.* Construction of MXene/Bi_2WO_6 Schottky junction for highly efficient piezocatalytic hydrogen evolution and unraveling mechanism. *Nano Lett* 2024, **24**: 3361–3368.
[28] Zhu RX, Liu Q, He Y, *et al.* Rapid construction of nickel phyllosilicate with ultrathin layers and high performance for CO_2 methanation. *J Colloid Interf Sci* 2024, **668**: 352–365.
[29] Zhou YG, Zhang YF, Lin MS, *et al.* Monolayered Bi_2WO_6 nanosheets mimicking heterojunction interface with open surfaces for photocatalysis. *Nat Commun* 2015, **6**: 8340.
[30] Li SG, Bai LQ, Ji N, *et al.* Ferroelectric polarization and thin-layered structure synergistically promoting CO_2 photoreduction of Bi_2MoO_6. *J Mater Chem A* 2020, **8**: 9268–9277.
[31] Pang B, Liu SC, Tu Y, *et al.* Controllable synthesis and enhanced photoactivity of two-dimensional Bi_2WO_6Ultra-thin nanosheets. *ChemistrySelect* 2021, **6**: 5381–5386.
[32] Chinh VD, Broggi A, Di Palma L, *et al.* XPS spectra analysis of Ti^{2+}, Ti^{3+} ions and dye photodegradation evaluation of titania-silica mixed oxide nanoparticles. *Journal Elec Materi* 2018, **47**: 2215–2224.
[33] Xu XL, Xiao LB, Zhao J, *et al.* Molecular ferroelectrics-driven high-performance perovskite solar cells. *Angew Chem Int Ed* 2020, **59**: 19974–19982.
[34] Komljenovic R, Sherrell PC, Goudeli E, *et al.* Piezo-to-piezo (P2P) conversion: Simultaneous β-phase crystallization and poling of ultrathin, transparent and freestanding homopolymer PVDF films*via*MHz-order nanoelectromechanical vibration. *Mater Horiz* 2025, **12**: 1207–1222.
[35] Xu XL, Wang Y, Cheng WW, *et al.* Defect dipole alignment mediated by poling for simultaneous optimization of piezoelectricity and carrier concentration in piezocatalysts. *Commun Chem* 2026, **9**: 22.
[36] Su R, Wang ZP, Zhu LN, *et al.* Strain-engineered nano-ferroelectrics for high-efficiency piezocatalytic overall water splitting. *Angew Chem Int Ed* 2021, **60**: 16019–16026.
[37] Li YR, Zhang XL, Li T, *et al.* Few-layer oxygen vacant $Bi_2O_2(OH)NO_3$ for dual-channel piezocatalytic H_2O_2 production from H_2O and air. *Chin J Catal* 2025, **75**: 105–114.
[38] Liu LZ, Hu JC, Ma ZY, *et al.* One-dimensional single atom arrays on ferroelectric nanosheets for enhanced CO_2 photoreduction. *Nat Commun* 2024, **15**: 305.
[39] Xu LY, Ouyang J, Cheng ZX, *et al.* A review on the dielectric ceramics for high energy-storage application. *Adv Ceram* 2025, **46**: 195–246. (in Chinese)
[40] Sha N, Bala HR, Zhang BW, *et al.* Surface passivation by CTAB toward highly efficient and stable perovskite solar cells. *Appl Surf Sci* 2023, **635**: 157643.
[41] Wang CY, Tu SC, Chen F, *et al.* Asymmetric single-unit-cell layer enriching polar inherent hydroxyls eliminates interlayer electric field shielding effect and *in situ* self-polarize for piezocatalytic water splitting. *Adv Mater* 2025, **37**: 2505592.
[42] Hu C, Hu JC, Zhu ZJ, *et al.* Orthogonal charge transfer by precise positioning of silver single atoms and clusters on carbon nitride for efficient piezocatalytic pure water splitting. *Angew Chem Int Ed* 2022, **61**: 202212397.
[43] Tian G, Deng WL, Yang T, *et al.* Insight into interfacial polarization for enhancing piezoelectricity in ferroelectric nanocomposites. *Small* 2023, **19**: 2207947.
[44] Yu Q, Sun SH, Jin XM, *et al.* Type-I heterojunction photocatalysis: Enhanced activity via $ZnIn_2S_4$/$MnCo_2O_{4.5}$ interfacial electric fields. *Chin J Struct Chem* 2025, **44**: 100620.
[45] Cheng WW, Xu XL, Zhai H, *et al.* Composition-tuned piezoelectricity governs hydrogen evolution in $Ba_{1-x}Sr_xTiO_3$ ($0 \le x \le 0.3$). *Adv Funct Mater* 2025: 16480.
[46] Zhang TY, Zhou P, Simon T, *et al.* Internal flow in sessile droplets induced by substrate oscillation: Towards enhanced mixing and mass transfer in microfluidic systems. *Microsyst Nanoeng* 2024, **10**: 86.
[47] Berr MJ, Wagner P, Fischbach S, *et al.* Hole scavenger redox potentials determine quantum efficiency and stability of Pt-decorated CdS nanorods for photocatalytic hydrogen generation. *Appl Phys Lett* 2012, **100**: 223903.
[48] You HL, Wu Z, Zhang LH, *et al.* Harvesting the vibration energy of $BiFeO_3$ nanosheets for hydrogen evolution. *Angew Chem Int Ed* 2019, **58**: 11779–11784.
[49] Xu XL, Cheng WW, Zhai H, *et al.* Toward enhanced pyro-catalysis performance: Mechanisms, strategies and challenges. *J Mater Chem A* 2025, **13**: 14465–14490.
[50] Bharatvaj J, Preethi V, Kanmani S. Hydrogen production from sulphide wastewater using Ce^{3+}–TiO_2 photocatalysis. *Int J Hydrog Energy* 2018, **43**: 3935–3945.
[51] Xu XL, Xiao LB, Jia YM, *et al.* Pyro-catalytic hydrogen evolution by $Ba_{0.7}Sr_{0.3}TiO_3$ nanoparticles: Harvesting cold–hot alternation energy near room-temperature. *Energy Environ Sci* 2018, **11**: 2198–2207.
[52] Wang K, Han C, Li JQ, *et al.* The mechanism of piezocatalysis: Energy band theory or screening charge effect. *Angew Chem Int Ed* 2022, **61**: 202110429.
[53] Zhang T, Luo HM, Abdi-Jalebi M, *et al.* Perovskite solar cells with ferroelectricity. *Inf Funct Mater* 2024, **1**: 87–107.
[54] Ma JP, Xiong X, Wu D, *et al.* Band position-independent piezo-electrocatalysis for ultrahigh CO_2 conversion. *Adv Mater* 2023, **35**: 2300027.
[55] Ren ZR, Chen F, Zhao Q, *et al.* Efficient CO_2 reduction to reveal the piezocatalytic mechanism: From displacement current to active sites. *Appl Catal B Environ* 2023, **320**: 122007.

[56] Xiao LB, Xu XL, Jia YM, *et al.* Pyroelectric nanoplates for reduction of CO_2 to methanol driven by temperature-variation. *Nat Commun* 2021, **12**: 318.
[57] Yang MM, Kim DJ, Alexe M. Flexo-photovoltaic effect. *Science* 2018, **360**: 904–907.
[58] Wu T, Liu K, Liu SH, *et al.* Highly efficient flexocatalysis of two-dimensional semiconductors. *Adv Mater* 2023, **35**: 2208121.
[59] Fu YH, Xu ZC, Liu HR, *et al.* Disrupt mitochondrial proton gradients via flexoelectric catalysis to deplete tumor energy and enhance immunotherapy. *Adv Funct Mater* 2025, **35**: 2421302.
[60] Cao JL, Jia YM, Wan XM, *et al.* Strong tribocatalysis of strontium titanate nanofibers through harvesting friction energy for dye decomposition. *Ceram Int* 2022, **48**: 9651–9657.
[61] Wang ZM, Dong XL, Tang W, *et al.* Contact-electro-catalysis (cec). *Chem Soc Rev* 2024, **53**: 4349–4373.
[62] Li PC, Wu J, Wu Z, *et al.* Strong tribocatalytic dye decomposition through utilizing triboelectric energy of barium strontium titanate nanoparticles. *Nano Energy* 2019, **63**: 103832.
[63] Wang ZM, Dong XL, Wu N, *et al.* A generalized approach for enhancing contact-electro-catalysis of oxides in a broad temperature range by fluorination. *Nat Commun* 2025, **16**: 11035.
[64] Jin CC, Cai YX, Shi KQ, *et al.* Hydrophilic/hydrophobic composite catalysts to enhance contact-electro-catalytic performance of polytetrafluoroethylene. *Small* 2025, **21**: 2503004.
[65] Lei H, Wu Z, Wang HB, *et al.* Converting H_2O and CO_2 into chemical fuels by nickel via friction. *Surf Interfaces* 2024, **46**: 104203.